ACS APPLIED MATERIALS & INTERFACES

Research Article

www.acsami.org

Aqueous-Processed Inorganic Thin-Film Solar Cells Based on $CdSe_xTe_{1-x}$ Nanocrystals: The Impact of Composition on Photovoltaic Performance

Qingsen Zeng,[†] Zhaolai Chen,[†] Yue Zhao,[‡] Xiaohang Du,[†] Fangyuan Liu,[†] Gan Jin,[†] Fengxia Dong,[†] Hao Zhang,[†] and Bai Yang*[,†]

[†]State Key Laboratory of Supramolecular Structure and Materials, College of Chemistry, and [‡]State Key Laboratory of Inorganic Synthesis and Preparative Chemistry, College of Chemistry, Jilin University, Changchun, 130012, P. R. China

Supporting Information

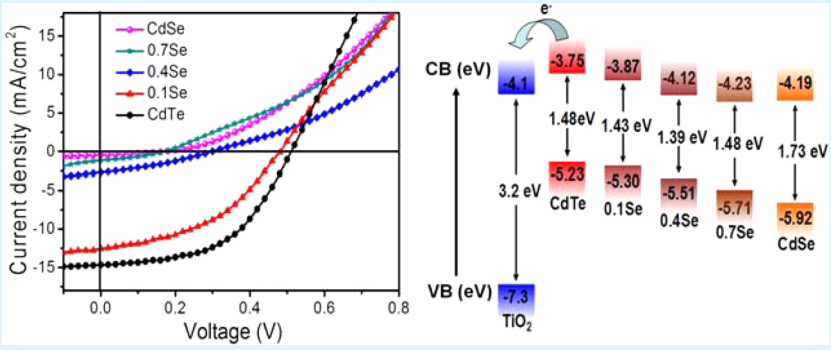

ABSTRACT: Aqueous processed nanocrystal (NC) solar cells are attractive due to their environmental friendliness and cost effectiveness. Controlling the bandgap of absorbing layers is critical for achieving high efficiency for single and multijunction solar cells. Herein, we tune the bandgap of CdTe through the incorporation of Se via aqueous process. The photovoltaic performance of aqueous $CdSe_xTe_{1-x}$ NCs is systematically investigated, and the impacts of charge generation, transport, and injection on device performance for different compositions are deeply discussed. We discover that the performance degrades with the increasing Se content from CdTe to CdSe. This is mainly ascribed to the lower conduction band (CB) of $CdSe_xTe_{1-x}$ with higher Se content, which reduces the driving force for electron injection into TiO_2. Finally, the performance is improved by mixing $CdSe_xTe_{1-x}$ NCs with conjugated polymer poly(*p*-phenylenevinylene) (PPV), and power conversion efficiency (PCE) of 3.35% is achieved based on ternary NCs. This work may provide some information to further optimize the aqueous-processed NC and hybrid solar cells.

KEYWORDS: *nanocrystal, solar cell, aqueous process, $CdSe_xTe_{1-x}$, CdTe, electron injection, hybrid*

INTRODUCTION

Solution-processed inorganic NC photovoltaics have attracted increasing attention over the past decade due to the tunable bandgap, excellent photoelectric properties and good photostability of NCs.[1−10] Meanwhile, a number of NCs have been investigated for fabricating inorganic NC solar cells. Generally, these NCs can be divided into two categories. One is nanocrystalline bulk semiconductor, such as CdTe, Cu(In,Ga)$(SeS)_2$, and $Cu_2ZnSn(SeS)_4$.[11−13] The other is the quantum-confined system, such as PbS, PbSe, and PbS_xSe_{1-x}.[14−17] The photovoltaic performance of NC solar cells has achieved great progress in recent years. Recently, a PCE of 8−9% was achieved for NC solar cells through optimizing materials properties and device structure.[18−20]

Ideally the solution-processed inorganic NC solar cells should be manufactured in an environmentally friendly way. Therefore, aqueous-processed photovoltaic devices provide a promising approach to fabricate NC solar cells. Recently, Yang et al. constructed pure inorganic solar cells utilizing the aqueous CdTe NCs, which achieved a high PCE approaching 4%.[21] Nevertheless, the bandgap of CdTe is constant due to the necessary thermal treatment to the active layers to achieve large crystal growth, which makes the crystal size exceed the Exciton Bohr radius. The Shockley−Queisser limit for single and multijunction solar cells dictates that controlling the bandgap of absorbing layers is important for achieving high efficiency.[22,23] According to the work of Mulvaney et al.,[24,25] one approach to bandgap tuning of CdTe is through the incorporation of Se to create ternary $CdSe_xTe_{1-x}$ alloys.

In this work, aqueous 2-mercaptoethylamine (MA) capped $CdSe_xTe_{1-x}$ NCs are synthesized by direct injection of $NaHSe_xTe_{1-x}$ into Cd precursor solution. And the photovoltaic

Received: August 5, 2015
Accepted: October 5, 2015
Published: October 5, 2015

DOI: 10.1021/acsami.5b07197
ACS Appl. Mater. Interfaces 2015, 7, 23223−23230

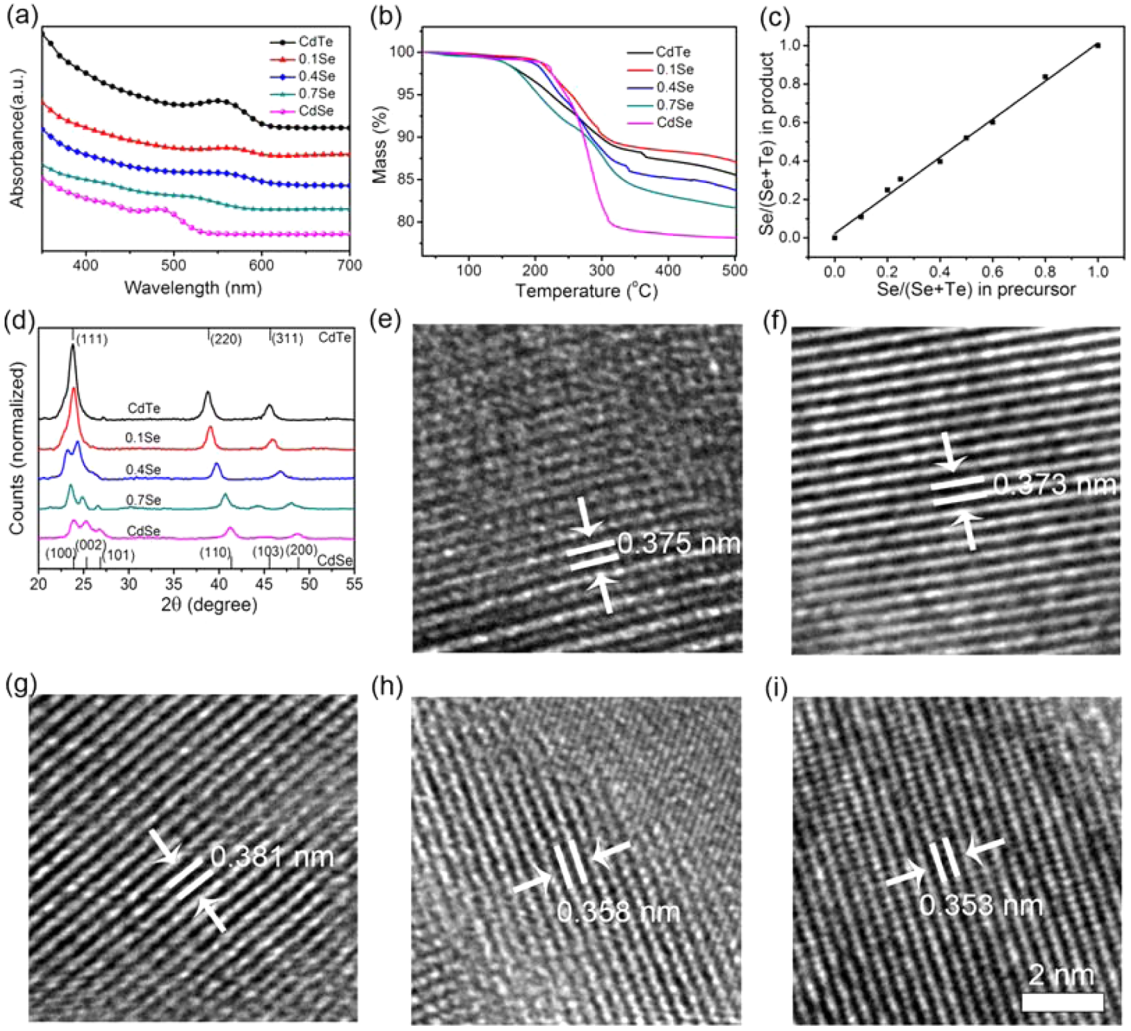

Figure 1. (a) Absorption spectra of $CdSe_xTe_{1-x}$ NCs film on quartz substrate. (b) TGA curve of $CdSe_xTe_{1-x}$ NCs. (c) Energy disperse spectroscopy is used to measure the relative amount of selenium in the sintered film versus the relative amount of selenium in the precursor injection solution. (d) X-ray diffraction patterns of $CdSe_xTe_{1-x}$ film annealed at 315 °C for 15 min in the glovebox. (e–i) HR-TEM images of CdTe (e), 0.1Se (f), 0.4Se (g), 0.7Se (h), and CdSe (i) NCs annealed at 315 °C.

performance of aqueous $CdSe_xTe_{1-x}$ NCs is systematically investigated utilizing the inverted device structure of ITO/TiO_2/$CdSe_xTe_{1-x}$/MoO_3/Au. We discover that the device performance degrades with the increasing Se content from CdTe to CdSe. This is mainly ascribed to the lower CB of $CdSe_xTe_{1-x}$ with higher Se content, which reduces the driving force for electron injection into TiO_2. Finally, the device performance is well improved by mixing $CdSe_xTe_{1-x}$ NCs with conjugated polymer PPV and PCE of 3.35% is achieved.

EXPERIMENTAL METHODS

Materials. Tellurium powder (200 mesh, 99.8%), selenium powder (100 mesh, 99.99%), R, R0-dichloro-*p*-xylene (98%), and tetrahydrothiophene (99%) were all purchased from Aldrich. 2-Mercaptoethylamine (MA, 98%) was obtained from Acros. Sodium borohydride ($NaBH_4$, 96%) was purchased from Sinopharm Group Co. Ltd. $CdCl_2$ (98%) was commercially available. All chemicals were used as received.

Preparation of $CdSe_xTe_{1-x}$ NCs. $CdSe_xTe_{1-x}$ NCs were prepared in a similar way to our previous work.[26] In brief, freshly prepared $NaHSe_xTe_{1-x}$ solution was injected into N_2-saturated $CdCl_2$ solution in the presence of MA in the pH range 5.70–5.74. The molar ratio of Cd/MA/(Te + Se) was set as 1:2.4:0.2. The resultant precursor solution was refluxed for 55 min to maintain the growth of $CdSe_xTe_{1-x}$ NCs. After that, the NCs solution was centrifuged at 8000 rpm for 3 min after adding isopropanol to remove excessive MA and superfluous salts. Subsequently, the NCs were dried in a vacuum oven and then dissolved in deionized water. The final concentration of the $CdSe_xTe_{1-x}$ NCs was 120 mg mL^{-1}.

Preparation of PPV. The synthesis method of PPV precursor could be found elsewhere.[27] In brief, 10 mL 0.4 M NaOH was added into 10 mL 0.4 M *p*-xylylenebis (tetrahydrothiophenium chloride) methanol solution. This solution was cooled to 0–5 °C in an ice bath. The reaction proceeded for 1 h and then was terminated by the addition of 0.4 M HCl aqueous solution to neutralize the reaction solution. The PPV precursor solution was dialyzed in deionized water for 1 week. The solution concentration of PPV precursor in this case was measured to be 5 mg mL^{-1}.

Device Fabrication. The indium tin oxide (ITO) was cleaned using chloroform, acetone, isopropanol and ethanol before drying in a N_2 flow. Next, the ITO substrate was immediately coated with the TiO_2 precursor at a speed of 2000 rpm for 10 s. Afterward, the samples were annealed for 20 min at 450 °C to convert the TiO_2 precursor into anatase-phase TiO_2. The active layer was fabricated by spin-coating the blended solution or $CdSe_xTe_{1-x}$ NCs solution at a speed of 700 rpm for 1 min. The first layer was annealed for 2 min at 315 °C in the glovebox before spin coating the second layer which was annealed for 15 min for pure inorganic devices or 60 min for hybrid devices, respectively, at 315 °C in the glovebox. Finally, a 5 nm MoO_3 film and

DOI: 10.1021/acsami.5b07197
ACS Appl. Mater. Interfaces 2015, 7, 23223–23230

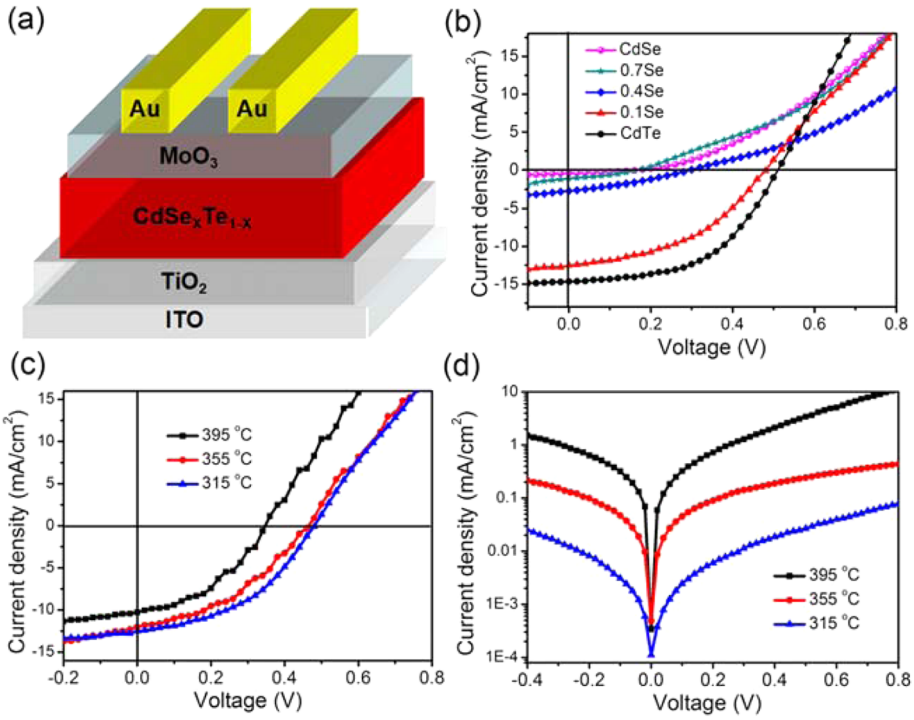

Figure 2. (a) Device structure and (b) J-V characteristics of the inorganic $CdSe_xTe_{1-x}$ NC solar cells. (c) *J*−*V* characteristics of 0.1Se NC solar cell annealing at different temperature under AM1.5G illumination. (d) *J*−*V* characteristics of 0.1Se NC solar cell annealing at different temperature in the dark.

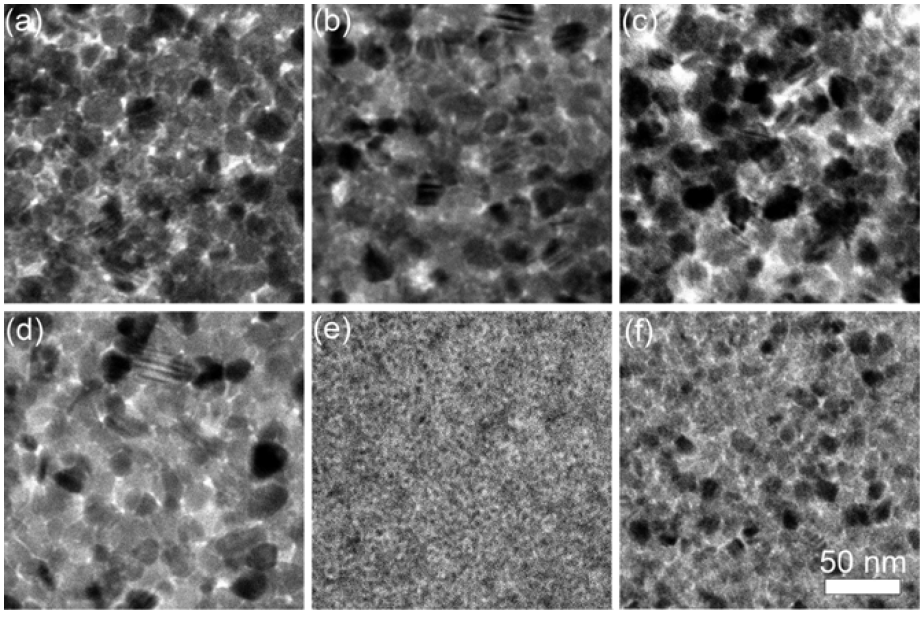

Figure 3. TEM images of CdTe (a), 0.1Se (b), 0.4Se (c), 0.7Se (d), CdSe (e) NCs annealed at 315 °C, and CdSe NCs (f) annealed at 355 °C.

a 60 nm gold electrode were evaporated through a mask at a pressure below 10^{-5} Torr, leading to an active area of 0.05 cm^2.

Characterization. UV−visible absorption spectra were obtained using a Shimadzu 3600 UV−visible-NIR spectrophotometer. Atomic force microscopy (AFM) micrographs were recorded in tapping mode with a Nanoscope IIIa scanning probe microscope from Digital Instruments. Transmission electron microscopy (TEM) was conducted using a Hitachi H-800 electron microscope at an acceleration voltage of 200 kV with a CCD camera. Thermal gravity analysis (TGA) was studied with a Q500 thermalgravimetric analyzer (American TA Company). Energy disperse spectroscopy (EDS-SEM) data were collected on 1um thick $CdSe_xTe_{1-x}$ films after annealing at 315 °C using Bruker energy disperse spectroscopy, the scanning area is a few square millimeters. XRD data were collected on 240 nm thick $CdSe_xTe_{1-x}$ films annealing at 315 °C for 15 min using a PANalytical B.V.-Empyream Diffractometer with Cu Kα radiation. Current density versus voltage (*J*−*V*) characteristics were measured by a computer-controlled Keithley 2400 source meter measurement system under 100 mW/cm^2 illumination with an AM1.5G filter. The incident photon to current efficiency (IPCE) was recorded under illumination of monochromatic light from the halogen tungsten lamp using a monochromator (Newport IQE 200) and detected by a computer-controlled lock-in amplifier. The electrochemical impedance spectra (EIS) measurements were conducted from a CHI 660E

DOI: 10.1021/acsami.5b07197
ACS Appl. Mater. Interfaces 2015, 7, 23223−23230

Table 1. Photovoltaic Performance of Optimized $CdSe_xTe_{1-x}$ NC Solar Cells, under the Illumination of AM1.5G, 100 mW cm^{-2}

sample	J_{sc} (mA cm^{-2})	V_{oc} (V)	FF	PCE (%)
CdTe	13.94 (±0.16)	0.513 (±0.01)	0.513 (±0.01)	3.67 (±0.17)
0.1Se	12.87 (±0.35)	0.457 (±0.03)	0.423 (±0.02)	2.48 (±0.17)
0.4Se	2.66 (±0.23)	0.312 (±0.01)	0.317 (±0.02)	0.263 (±0.03)
0.7Se	1.20 (±0.15)	0.170 (±0.01)	0.319 (±0.01)	0.059 (±0.01)
CdSe	0.40 (±0.06)	0.189 (±0.02)	0.307 (±0.02)	0.024 (±0.002)

Table 2. Photovoltaic Performance of Ternary 0.1Se NC Solar Cells Annealed at Different Temperature, under the Illumination of AM1.5G, 100 mW cm^{-2}

annealing temperature	J_{sc} (mA cm^{-2})	V_{oc} (V)	FF	PCE (%)
315 °C	12.87 (±0.35)	0.457 (±0.03)	0.423 (±0.02)	2.48 (±0.17)
355 °C	11.91 (±0.66)	0.441 (±0.04)	0.401 (±0.01)	2.11 (±0.37)
395 °C	10.22 (±0.11)	0.348 (±0.01)	0.404 (±0.02)	1.44 (±0.07)

electrochemical workstation in dark conditions at zero bias voltage with a frequency ranging from 1 Hz to 100 kHz.

RESULT AND DISCUSSION

Synthesis and Characterization of $CdSe_xTe_{1-x}$ NCs. For optical characterization, the $CdSe_xTe_{1-x}$ NCs is spun onto quartz substrate. Alloyed NCs with different compositions show different absorbance spectra (Figure 1a). The red shifts of the first excitonic peaks of $CdSe_{0.1}Te_{0.9}$ (0.1Se) and $CdSe_{0.4}Te_{0.6}$ (0.4Se) NCs compared to the pristine CdTe NCs are due to the "optical bowing" effects.[28] In addition, CdSe and CdTe NCs show more obvious first excitonic peaks compared to the ternary NCs which is attributed to the much wider size distribution of the ternary NCs (Figure S1). From the TEM images, we know the size of as-prepared $CdSe_xTe_{1-x}$ NCs ranges from 2 to 5 nm with an average diameter of ~3 nm.

Now we turn our attention to understanding the properties of $CdSe_xTe_{1-x}$ NCs after annealing, which are closely related to the photovoltaic performance. Thermal gravity analysis (TGA) is carried out to to elucidate the thermal decomposition process of the alloyed NCs. The results presented in Figure 1b show that there is one obvious slope corresponding to the removal of the ligands on the surface of NCs. The decomposition of ligands starts at 150−200 °C for alloyed NCs. When

Table 3. Hole Mobility of CdTe, 0.1Se, 0.4Se, 0.7Se, CdSe NCs Annealed at 315 °C and CdSe NCs Annealed at 355 °C

sample	hole mobility (cm^2 V^{-1} s^{-1})
CdTe	1.34 (±0.96) × 10^{-5}
0.1Se	5.42 (±1.08) × 10^{-6}
0.4Se	5.33 (±0.84) × 10^{-6}
0.7Se	1.77 (±1.13) × 10^{-5}
CdSe	4.30 (±1.21) × 10^{-8}
CdSe-355 °C	6.88 (±1.35) × 10^{-4}

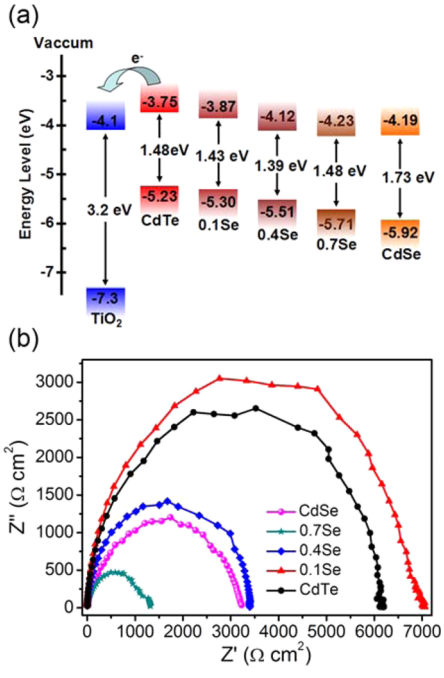

Figure 4. (a) Schematic energy level diagram of TiO_2 and sintered CdTe, 0.1Se, 0.4Se, 0.7Se, and CdSe NCs. (b) Electrochemical impedance spectra of the five cells characterized at the bias of 0 V in the dark.

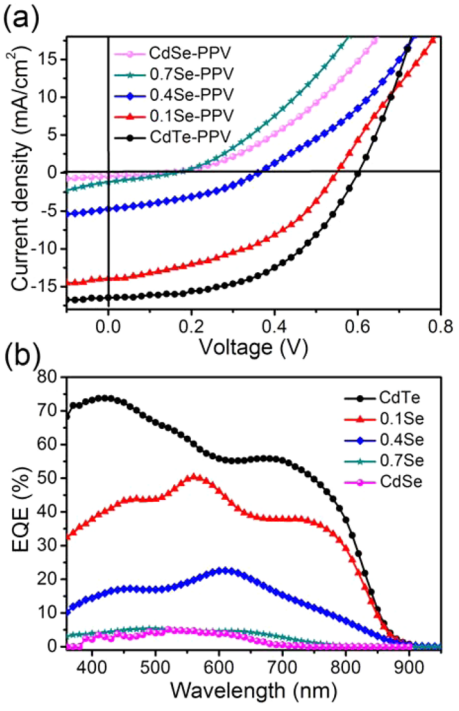

Figure 5. (a) $J-V$ characteristics and (b) external quantum efficiency curves of PPV/$CdSe_xTe_{1-x}$ HSCs.

DOI: 10.1021/acsami.5b07197
ACS Appl. Mater. Interfaces 2015, 7, 23223−23230

Table 4. Photovoltaic Performance of Optimized PPV/$CdSe_xTe_{1-x}$ HSCs, under the Illumination of AM1.5G, 100 mW cm^{-2}

sample	J_{sc} (mA cm^{-2})	V_{oc} (V)	FF	PCE (%)
CdTe-PPV	16.94 (±0.62)	0.582 (±0.02)	0.490 (±0.01)	4.83 (±0.14)
0.1Se-PPV	13.94 (±0.61)	0.552 (±0.01)	0.415 (±0.02)	3.22 (±0.15)
0.4Se-PPV	4.58 (±0.14)	0.356 (±0.01)	0.370 (±0.01)	0.619 (±0.02)
0.7Se-PPV	1.21 (±0.12)	0.194 (±0.02)	0.311 (±0.02)	0.073 (±0.008)
CdSe-PPV	0.53 (±0.03)	0.233 (±0.02)	0.307 (±0.01)	0.038 (±0.006)

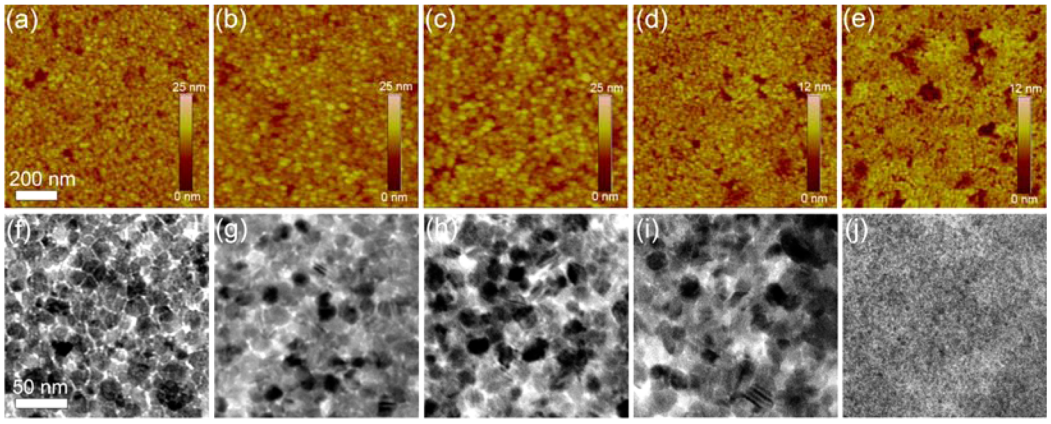

Figure 6. (a–e and f–j) AFM and TEM images of the PPV/$CdSe_xTe_{1-x}$ blend layer, respectively. All samples are spun cast from a solution of PPV/$CdSe_xTe_{1-x}$ for CdTe (a, f); 0.1Se (b, g); 0.4Se (c, h); 0.7Se (d, i); CdSe (e, j).

temperature reaches up to 310 °C, the ligands are removed almost completely.

Energy disperse spectroscopy (EDS-SEM) is used to investigate the anionic ratio of alloyed NCs after annealing at 315 °C. Figure 1c shows the results from EDS data taken on a series of samples where the relative amount of Se in the precursor (Se/(Se + Te)) varies from 0 to 1. It is worth noting that the Se/(Se + Te) ratio in the annealed NCs films is same as that in the precursor solution. This is different from the reported $CdSe_xTe_{1-x}$ NCs which were synthesized through the incorporation of selenium anions into CdTe NCs.[29] Presumably, the phenomenon is attributed to the high reaction activity of Se and Te precursor as well as the excessive Cd ions in the reaction system.

XRD is implemented to study the crystal structure of sintered $CdSe_xTe_{1-x}$ film, as exhibited in Figure 1d. All the samples are crystalline well over the range of the composition parameters. The CdSe and CdTe films display their thermodynamically most stable hexagonal and cubic crystal phases, respectively.[24] In addition, the peaks of Te rich sample (0.1Se) shift to higher 2θ values with increasing Se content, which is consistent with the formation of an alloyed cubic phase that possesses an increasingly smaller lattice constant. These observations agree well with previous reports on bulk alloyed $CdSe_xTe_{1-x}$.[30,31] To further confirm the homogeneous alloyed phase of sintered $CdSe_xTe_{1-x}$ NCs, the high-resolution TEM (HR-TEM) characterization is conducted. As shown in Figure 1e–i, the uniform lattice structure suggests that the Te and Se anions are uniformly distributed within the alloyed nanoparticles. The interplanar distance of 3.75, 3.73, 3.81, 3.58, and 3.53 Å corresponds to the (111) crystallographic facet of cubic CdTe and 0.1Se, the (100) crystallographic facet of hexagonal 0.4Se, and (002) crystallographic facet of hexagonal 0.7Se and CdSe, respectively. These agree well with the XRD results.

Photovoltaic Performance. NC solar cells are fabricated by using our previously reported inverted structure of ITO/TiO_2 (30 nm)/$CdSe_xTe_{1-x}$ (160 nm)/MoO_3 (5 nm)/Au (60 nm), as presented in Figure 2a. TiO_2 and MoO_3 are selected as electron transport layer and hole transport layer, respectively. The active layers are annealed at 315 °C for 15 min, at which temperature the ligands are removed completely. The CdTe, 0.1Se, 0.4Se and $CdSe_{0.7}Te_{0.3}$ (0.7Se) NCs after annealing show similar size distributions with average sizes of approximate 20 nm (Figure 3a-d). Though the ligands of CdSe NCs have been removed at 315 °C, the crystal growth is not obvious (Figure 3e) which is mainly due to the larger lattice energy of CdSe (749 kcal/mol) compared to CdTe (680 kcal/mol).[32] This is confirmed by the result that the sizes of CdSe NCs can reach about 15 nm when raising the annealing temperature to 355 °C (Figure 3f).

The current density–voltage curves of the optimized photovoltaic devices for each NCs are shown in Figure 2b, and the detailed photovoltaic parameters are listed in Table 1. The champion device employing CdTe NCs exhibits a short circuit current density (J_{sc}) of 14.67 mA/cm^2, an open circuit voltage (V_{oc}) of 0.512 V, a fill factor (FF) of 51.1%, and a high PCE of 3.83%. In the devices based on ternary $CdSe_xTe_{1-x}$ NCs, the $CdSe_{0.1}Te_{0.9}$ NC solar cells achieve the best PCE of 2.65% with the J_{sc} of 12.52 mA/cm^2, V_{oc} of 0.482 V, and FF of 43.9%. It is noting that almost all device parameters, especially the J_{sc}, decrease with increasing Se content, thus resulting in a decreasing PCE regularly. In general, the quality of $CdSe_xTe_{1-x}$ NCs correlates intimately with annealing temperature. Elevated temperature can increase the crystal size, which improve the carrier mobility. Therefore, the influence of temperature on device performance is investigated with the 0.1Se NCs. However, the device performance degrades with increase of temperature (Figure 2c, Table 2), which is mainly ascribed to the reduced V_{oc}. As presented in Figure 2d, the solar cells annealed at higher temperature display a larger dark current. That is, the elevated temperature increases the leakage current, thus leading to decreased device performance. As shown in

DOI: 10.1021/acsami.5b07197
ACS Appl. Mater. Interfaces 2015, 7, 23223–23230

Figure S2, the size of voids between NCs increases with the increase of temperature. This will increase the leakage current which in turn lowers the V_{oc}.

The essence of photovoltaic cells is the charge generation, transport, and injection. To deeply understand the variation of the device performance, the impacts of Se content on the three aspects are systematically investigated in the following part.

Charge Generation. The charge generation efficiency is determined by the absorption yield and exciton dissolution yield. Since the size of annealed $CdSe_xTe_{1-x}$ NCs is larger than their exciton Bohr radius and the binding energy of the bulk counterparts is just tens of milli-electron volts, exciton dissolution is facile at room temperature for all the samples. For the absorption characterization of the annealed NCs films (Figure S3), we discover that the absorption slightly decreases with higher Se content, which will slightly reduce the photogenerated carriers and thus the J_{sc}. However, the slightly decreased optical absorption with higher Se content cannot account for the sharp decrease of the J_{sc}. In addition, the optical absorption usually has negligible effect on the V_{oc} and FF. As a consequence, the slightly decreased charge generation efficiency of the sintered NCs with higher Se content is not the key factor leading to the decreased device performance.

Charge Transport. To illustrate the reasons resulting in the decreasing photovoltaic performance with higher Se content, we measure the hole carrier mobility of $CdSe_xTe_{1-x}$ NCs after annealing by the space-charge-limited-current (SCLC) method to investigate the charge transport properties. The hole-only device structure is ITO/$CdSe_xTe_{1-x}$/MoO_3/Au. The carrier mobility is calculated according to eq 1:

$$J = 9\varepsilon_0\varepsilon_r\mu(V - V_{bi} - V_r)^2/8L^3 \quad (1)$$

where ε_0 is the permittivity of free space, ε_r is the dielectric constant of $CdSe_xTe_{1-x}$, μ is the hole mobility, V is the applied voltage, V_r is the voltage drop due to contact resistance and series resistance across the electrodes, V_{bi} is the built-in voltage, and L is the film thickness. As shown in Figure S4 and Table 3, the mobility is similar for the sintered NCs films except CdSe, which is consistent with their similar crystal size. The low mobility of CdSe NCs is ascribed to the insufficient growth which will increase the hopping process required for charge transport between NCs. When the annealing temperature is elevated to 355 °C, the further growth of CdSe NCs improves the hole mobility to 6.88×10^{-4} cm^2 V^{-1} s^{-1} (Figure S4f). Nevertheless, the performance improvement of CdSe NC solar cells is not distinct (Figure S5). Therefore, charge transport cannot account for the decreased device performance with higher Se content.

Charge Injection. A higher CB of NCs than TiO_2, which is beneficial to efficiently extract photogenerated electrons, is critical for achieving high performance of photovoltaic devices. This has been confirmed in colloidal quantum dot (CQD) sensitized solar cells and depleted heterojunction PbS CQD photovoltaics.[33−35] The larger the CB offset, the better the photogenerated electron injection.[36] The energy band of $CdSe_xTe_{1-x}$ NCs alters with the different Se content, which may affect the electron injection and thus the photovoltaic performance. The energy band diagram can be calculated based on previous report of Jasieniak and co-workers (calculated details see Figure S6),[24] schematically illustrated in Figure 4a. The CB and valence band (VB) decrease with increasing Se content. The decreased VB increases the VB offset between $CdSe_xTe_{1-x}$ and MoO_3 with higher Se content, which enhances the driving force for hole injection into MoO_3. Therefore, the hole transfer is independent of the decreased device performance.

As shown in Figure 4a, the CB edge of CdTe and 0.1Se NCs is higher than TiO_2, and correspondingly, these devices show better electron injection into TiO_2. However, the CB edge of 0.4Se, 0.7Se, and CdSe NCs with higher Se content is lower than TiO_2, which leads to adverse electron injection. The poor electron injection causes electron to accumulate in the TiO_2 electrode interface which will increase the recombination loss, thus causing the poor device performance. In the previous photovoltaic performance chapter, we notice that the devices of 0.7Se NCs have a lower V_{oc} than CdSe NCs. We speculate this result from the poorer electron injection due to the slightly lower CB edge of 0.7Se NCs than CdSe NCs. It is notable that though 0.7Se NCs have a poorer electron injection, the devices made of 0.7Se NCs still have a larger J_{sc} and FF than CdSe NC solar cells owing to the higher light absorption and carrier mobility of 0.7Se NCs.

Based on the above discussion, the performance of $CdSe_xTe_{1-x}$ NC solar cells is influenced by charge generation, transport, and injection comprehensively; however, the regular variation of photovoltaic performance with the composition of NCs mainly result from the electron injection depending on the CB edge of NCs. To further confirm this conclusion, electrochemical impedance spectra (EIS) is used to analyze the charge behavior dynamics. The EIS measurements are conducted in the dark condition at the bias of 0 V with a frequency ranging from 1 Hz to 100 kHz. As shown in Figure 4b, mainly one semicircle is observed on the Nyquist plot for each cell. The CdTe and 0.1Se NC solar cells show larger shunt resistance with about 6200 and 7100 Ω cm^2, respectively. And the 0.7Se NC solar cells show lowest shunt resistance with only 1400 Ω cm^2. The lower shunt resistance corresponds to the increased recombination loss. As a result, the charge recombination processes are obviously suppressed for CdTe and 0.1Se NC solar cells and favorable for 0.7Se NC solar cells, which agree well with the previous result.

Enhanced Performance via Mixing with PPV. More recently, we discovered the photovoltaic performance of aqueous-processed CdTe NC solar cells can be enhanced by mixing CdTe NCs with wide bandgap conjugated polymers, which can increase carrier lifetime, decrease leakage current and promote the interfacial carrier injection.[37] Therefore, the hybrid solar cells (HSCs) are fabricated by mixing $CdSe_xTe_{1-x}$ NCs with conjugated polymers PPV in the second active layer (device structure, see Figure S7). Due to the thermopolymerization property of PPV precursor,[38] a small amount of PPV is enough to form continuous pathway with optimized weight ratio of 2.1% and volume ratio about 12% in the hybrid film. As shown in Figure 5a, with the detailed photovoltaic parameters listed in Table 4, the introduction of PPV improves PCE efficiently compared to the pure inorganic $CdSe_xTe_{1-x}$ solar cells. And the photovoltaic performance of HSCs decreases with higher Se content, which is consistent with the performance of pure inorganic devices. In the devices fabricated with ternary $CdSe_xTe_{1-x}$ NCs and PPV, the champion device based on 0.1Se/PPV exhibits a J_{sc} of 13.94 mA/cm^2, a V_{oc} of 0.552 V, an FF of 43.5%, and a high PCE of 3.35%, which, to the best of our knowledge, is the highest for aqueous-processed polymer/NCs hybrid solar cells based on ternary NCs. The corresponding external quantum efficiency (EQE) curves are

DOI: 10.1021/acsami.5b07197
ACS Appl. Mater. Interfaces 2015, 7, 23223−23230

shown in Figure 5b. The decreasing EQE matches well with the decreasing J_{sc} with higher Se content.

The morphology of polymer/NCs hybrid films affects the charge separation and transport significantly. In general, the nanoscale morphology control of solution-processed polymer/NCs hybrid film is difficult due to the inferior miscibility of polymer and NCs. Mixed solvent is used to deal with this problem for organic-solvent-processed hybrid films;[39] however, the morphology control is still not perfect due to the different evaporation rate of the different solvent. Aqueous-processed hybrid films using the aqueous soluble polymer precursors and NCs can control the nanoscale morphology perfectly.[40−42] As show in Figure 6, the AFM and TEM measurements are implemented to investigate the surface and bulk morphology of $CdSe_xTe_{1-x}$ NCs and PPV hybrid films annealed at 315 °C, respectively. The hybrid films are very uniform and smooth with the root-mean-square (RMS) roughness ranging from 0.917 to 1.765 nm due to the appropriate phase segregation of NCs and PPV, which agrees well with the TEM images. The appropriate phase segregation increases the contact areas of the PPV and NCs, which increases the opportunity of charge transfer between PPV and NCs. In this case, prolonged carrier lifetime can be achieved which is beneficial for improving the photovoltaic performance.

CONCLUSIONS

In summary, we demonstrate the photovoltaic performance optimization of aqueous processed NC solar cells by tuning the bandgap of CdTe NCs through the incorporation of Se. The performance of $CdSe_xTe_{1-x}$ NC solar cells is influenced by charge generation, transport, and injection comprehensively; however, the photovoltaic performance is mainly determined by the electron injection. The better the electron injection, the higher the photovoltaic performance. Therefore, photovoltaic performance of $CdSe_xTe_{1-x}$ may be improved by enhancing the driving force for electron injection, which can be implemented via tuning the energy level of TiO_2 to increase the CB offset. Finally, the performance is well improved by mixing $CdSe_xTe_{1-x}$ NCs with conjugated polymer PPV and PCE of 3.35% is achieved.

ASSOCIATED CONTENT

Supporting Information

The Supporting Information is available free of charge on the ACS Publications website at DOI: 10.1021/acsami.5b07197.

Details of TEM images of the as-prepared $CdSe_xTe_{1-x}$ NCs and 0.1Se NCs annealed at different temperature, absorption spectra of the sintered $CdSe_xTe_{1-x}$ NCs, $J-V$ characteristics of the hole-only devices and CdSe solar cell annealed at 355 °C, the calculated details of bandgap and energy level, and the device structure of HSCs. (PDF)

AUTHOR INFORMATION

Corresponding Author

*Fax: +86 431 85193423. E-mail: byangchem@jlu.edu.cn.

Notes

The authors declare no competing financial interest.

ACKNOWLEDGMENTS

This work was financially supported by the National Science Foundation of China (NSFC) under Grant Nos. 51433003, 21221063, 91123031, 51373065, and the National Basic Research Program of China (973 Program) under Grant Nos. 2012CB933800 and 2014CB643503.

REFERENCES

(1) Sargent, E. H. Colloidal Quantum Dot Solar Cells. *Nat. Photonics* **2012**, *6*, 133−135.
(2) Tang, J.; Liu, H.; Zhitomirsky, D.; Hoogland, S.; Wang, X.; Furukawa, M.; Levina, L.; Sargent, E. H. Quantum Junction Solar Cells. *Nano Lett.* **2012**, *12*, 4889−4894.
(3) Lan, X.; Bai, J.; Masala, S.; Thon, S. M.; Ren, Y.; Kramer, I. J.; Hoogland, S.; Simchi, A.; Koleilat, G. I.; Paz-Soldan, D.; Ning, Z.; Labelle, A. J.; Kim, J. Y.; Jabbour, G.; Sargent, E. H. Self-Assembled, Nanowire Network Electrodes for Depleted Bulk Heterojunction Solar Cells. *Adv. Mater.* **2013**, *25*, 1769−1773.
(4) Li, L.; Coates, N.; Moses, D. Solution-Processed Inorganic Solar Cell Based on in Situ Synthesis and Film Deposition of $CuInS_2$ Nanocrystals. *J. Am. Chem. Soc.* **2010**, *132*, 22−23.
(5) Semonin, O. E.; Luther, J. M.; Choi, S.; Chen, H.-Y.; Gao, J.; Nozik, A. J.; Beard, M. C. Peak External Photocurrent Quantum Efficiency Exceeding 100% via MEG in a Quantum Dot Solar Cell. *Science* **2011**, *334*, 1530−1533.
(6) Etgar, L.; Zhang, W.; Gabriel, S.; Hickey, S. G.; Nazeeruddin, M. K.; Eychmüller, A.; Liu, B.; Grätzel, M. High Efficiency Quantum Dot Heterojunction Solar Cell Using Anatase (001) TiO_2 Nanosheets. *Adv. Mater.* **2012**, *24*, 2202−2206.
(7) Rath, A. K.; Bernechea, M.; Martinez, L.; de Arquer, F. P. G.; Osmond, J.; Konstantatos, G. Solution-Processed Inorganic Bulk Nano-Heterojunctions and Their Application to Solar Cells. *Nat. Photonics* **2012**, *6*, 529−534.
(8) Park, B.; Yun, S. H.; Cho, C. Y.; Kim, Y. C.; Shin, J. C.; Jeon, H. G.; Huh, Y. H.; Hwang, I.; Baik, K. Y.; Lee, Y. I.; Uhm, H. S.; Cho, G. S.; Choi, E. H. Surface Plasmon Excitation in Semitransparent Inverted Polymer Photovoltaic Devices and Their Applications as Label-Free Optical Sensors. *Light: Sci. Appl.* **2014**, *3*, e222.
(9) Kemp, K. W.; Labelle, A. J.; Thon, S. M.; Ip, A. H.; Kramer, I. J.; Hoogland, S.; Sargent, E. H. Interface Recombination in Depleted Heterojunction Photovoltaics Based on Colloidal Quantum Dots. *Adv. Energy Mater.* **2013**, *3*, 917−922.
(10) Ning, Z.; Voznyy, O.; Pan, J.; Hoogland, S.; Adinolfi, V.; Xu, J.; Li, M.; Kirmani, A. R.; Sun, J. P.; Minor, J.; Kemp, K. W.; Dong, H.; Rollny, L.; Labelle, A.; Carey, G.; Sutherland, B.; Hill, I.; Amassian, A.; Liu, H.; Tang, J.; Bakr, O. M.; Sargent, E. H. Air-Stable n-Type Colloidal Quantum Dot Solids. *Nat. Mater.* **2014**, *13*, 822−828.
(11) Jasieniak, J.; MacDonald, B. I.; Watkins, S. E.; Mulvaney, P. Solution-Processed Sintered Nanocrystal Solar Cells via Layer-by-Layer Assembly. *Nano Lett.* **2011**, *11*, 2856−2864.
(12) Panthani, M. G.; Akhavan, V.; Goodfellow, B.; Schmidtke, J. P.; Dunn, L.; Dodabalapur, A.; Barbara, P. F.; Korgel, B. A. Synthesis of CuInS2, CuInSe2, and Cu(InxGa1-x)Se_2 (CIGS) Nanocrystal "Inks" for Printable Photovoltaics. *J. Am. Chem. Soc.* **2008**, *130*, 16770−16777.
(13) Zhong, J.; Xia, Z.; Zhang, C.; Li, B.; Liu, X.; Cheng, Y. B.; Tang, J. One-Pot Synthesis of Self-Stabilized Aqueous Nanoinks for $Cu_2ZnSn(S,Se)_4$ Solar Cells. *Chem. Mater.* **2014**, *26*, 3573−3578.
(14) Zhang, J.; Gao, J.; Miller, E. M.; Luther, J. M.; Beard, M. C. Diffusion-Controlled Synthesis of PbS and PbSe Quantum Dots within Situ Halide Passivation for Quantum Dot Solar Cells. *ACS Nano* **2014**, *8*, 614−622.
(15) Luther, J. M.; Law, M.; Beard, M. C.; Song, Q.; Reese, M. O.; Ellingson, R. J.; Nozik, A. J. Schottky Solar Cells Based on Colloidal Nanocrystal Films. *Nano Lett.* **2008**, *8*, 3488−3492.
(16) Etgar, L.; Yanover, D.; Čapek, R. K.; Vaxenburg, R.; Xue, Z.; Liu, B.; Nazeeruddin, M. K.; Lifshitz, E.; Grätzel, M. Core/Shell PbSe/PbS QDs TiO_2 Heterojunction Solar Cell. *Adv. Funct. Mater.* **2013**, *23*, 2736−2741.

DOI: 10.1021/acsami.5b07197
ACS Appl. Mater. Interfaces 2015, 7, 23223−23230

(17) Ma, W.; Luther, J. M.; Zheng, H.; Wu, Y.; Alivisatos, A. P. Photovoltaic Devices Employing Ternary PbS_xSe_{1-x} Nanocrystals. *Nano Lett.* **2009**, *9*, 1699−1703.
(18) Panthani, M. G.; Kurley, J. M.; Crisp, R. W.; Dietz, T. C.; Ezzyat, T.; Luther, J. M.; Talapin, D. V. High Efficiency Solution Processed Sintered CdTe Nanocrystal Solar Cells: The Role of Interfaces. *Nano Lett.* **2014**, *14*, 670−675.
(19) Zhitomirsky, D.; Voznyy, O.; Levina, L.; Hoogland, S.; Kemp, K. W.; Ip, A. H.; Thon, S. M.; Sargent, E. H. Engineering Colloidal Quantum Dot Solids Within and Beyond the Mobility-Invariant Regime. *Nat. Commun.* **2014**, *5*, 3803.
(20) Chuang, C.-H. M.; Brown, P. R.; Bulović, V.; Bawendi, M. G. Improved Performance and Stability in Quantum Dot Solar Cells through Band Alignment Engineering. *Nat. Mater.* **2014**, *13*, 796−801.
(21) Chen, Z.; Zhang, H.; Zeng, Q.; Wang, Y.; Xu, D.; Wang, L.; Wang, H.; Yang, B. In Situ Construction of Nanoscale CdTe-CdS Bulk Heterojunctions for Inorganic Nanocrystal Solar Cells. *Adv. Energy Mater.* **2014**, *4*, 1400235.
(22) Shockley, W.; Queisser, H. J. Detailed Balance Limit of Efficiency of p-n Junction Solar Cells. *J. Appl. Phys.* **1961**, *32*, 510−519.
(23) Vos, A. D. Detailed Balance Limit of the Efficiency of Tandem Solar Cells. *J. Phys. D: Appl. Phys.* **1980**, *13*, 839−846.
(24) MacDonald, B. I.; Martucci, A.; Rubanov, S.; Watkins, S. E.; Mulvaney, P.; Jasieniak, J. J. Layer-by-Layer Assembly of Sintered $CdSe_xTe_{1-x}$ Nanocrystal Solar Cells. *ACS Nano* **2012**, *6*, 5995−6004.
(25) Bailey, R. E.; Nie, S. Alloyed Semiconductor Quantum Dots: Tuning the Optical Properties without Changing the Particle Size. *J. Am. Chem. Soc.* **2003**, *125*, 7100−7106.
(26) Du, X.; Chen, Z.; Li, Z.; Hao, H.; Zeng, Q.; Dong, C.; Yang, B. Dip-Coated Gold Nanoparticle Electrodes for Aqueous-Solution-Processed Large-Area Solar Cells. *Adv. Energy Mater.* **2014**, *4*, 1400135.
(27) Yu, W.; Zhang, H.; Fan, Z.; Zhang, J.; Wei, H.; Zhou, D.; Xu, B.; Li, F.; Tian, W.; Yang, B. Efficient Polymer/Nanocrystal Hybrid Solar Cells Fabricated from Aqueous Materials. *Energy Environ. Sci.* **2011**, *4*, 2831−2834.
(28) Feng, Z. C.; Becla, P.; Kim, L. S.; Perkowitz, S.; Feng, Y. P.; Poon, H. C.; Williams, K. P.; Pitt, G. D. Raman, Infrared, Photoluminescence and Theoretical-Studies of the II- VI- I Ternary CdSeTe. *J. Cryst. Growth* **1994**, *138*, 239−243.
(29) Liang, G.-X.; Gu, M.-M.; Zhang, J.-R.; Zhu, J.-J. Preparation and Bioapplication of High-Quality, Water-Soluble, Biocompatible, and Near-Infrared-Emitting CdSeTe Alloyed Quantum Dots. *Nanotechnology* **2009**, *20*, 415103.
(30) Muthukumarasamy, N.; Balasundaraprabhu, R.; Jayakumar, S.; Kannan, M. D. Investigations on Structural Phase Transition in Hot Wall Deposited $CdSe_xTe_{1-x}$ Thin Films. *Mater. Chem. Phys.* **2007**, *102*, 86−91.
(31) More, P. D.; Shahane, G. S.; Deshmukh, L. P.; Bhosale, P. N. Spectro-Structural Characterisation of $CdSe_{1-x}Te_x$ Alloyed Thin Films. *Mater. Chem. Phys.* **2003**, *80*, 48−54.
(32) Zhao, X.; Wanga, X.; Lin, H.; Wang, Z. Relationships between Lattice Energy and Electronic Polarizability of ANB8-N Crystals. *Opt. Commun.* **2010**, *283*, 1668−1673.
(33) Mora-Sero, I.; Bisquert, J. Breakthroughs in the Development of Semiconductor-Sensitized Solar Cells. *J. Phys. Chem. Lett.* **2010**, *1*, 3046−3052.
(34) Braga, A.; Gimenez, S.; Concina, I.; Vomiero, A.; Mora-Sero, I. Panchromatic Sensitized Solar Cells Based on Metal Sulfide Quantum Dots Grown Directly on Nanostructured TiO_2 Electrodes. *J. Phys. Chem. Lett.* **2011**, *2*, 454−460.
(35) Liu, H.; Tang, J.; Kramer, I. J.; Debnath, R.; Koleilat, G. I.; Wang, X.; Fisher, A.; Li, R.; Brzozowski, L.; Levina, L.; Sargent, E. H. Electron Acceptor Materials Engineering in Colloidal Quantum Dot Solar Cells. *Adv. Mater.* **2011**, *2*, 3832−3837.
(36) Wang, D. F.; Zhao, H. G.; Wu, N. Q.; El Khakani, M. A.; Ma, D. L. Tuning the Charge-Transfer Property of PbS-Quantum Dot/TiO_2-Nanobelt Nanohybrids via Quantum Confinement. *J. Phys. Chem. Lett.* **2010**, *1*, 1030−1035.
(37) Chen, Z.; Liu, F.; Zeng, Q.; Cheng, Z.; Du, X.; Jin, G.; Zhang, H.; Yang, B. Efficient Aqueous-Processed Hybrid Solar Cells from a Polymer with a Wide Bandgap. *J. Mater. Chem. A* **2015**, *3*, 10969−10975.
(38) Liang, W. B.; Lenz, R. W.; Karasz, F. E. Poly(2-methoxyphenylene vinylene): Synthesis, Electrical Conductivity, and Control of Electronic Properties. *J. Polym. Sci., Part A: Polym. Chem.* **1990**, *28*, 2867−2875.
(39) Huynh, W. U.; Dittmer, J. J.; Libby, W. C.; Whiting, G. L.; Alivisatos, A. P. Controlling the Morphology of Nanocrystal-Polymer Composites for Solar Cell. *Adv. Funct. Mater.* **2003**, *13*, 73−79.
(40) Chen, Z.; Zhang, H.; Xing, Z.; Hou, J.; Li, J.; Wei, H.; Tian, W.; Yang, B. Aqueous-Solution-Processed Hybrid Solar Cells with Good Thermal and Morphological Stability. *Sol. Energy Mater. Sol. Cells* **2013**, *109*, 254−261.
(41) Chen, Z.; Zhang, H.; Yu, W.; Li, Z.; Hou, J.; Wei, H.; Yang, B. Inverted Hybrid Solar Cells from Aqueous Materials with a PCE of 3.61%. *Adv. Energy Mater.* **2013**, *3*, 433−437.
(42) Jin, G.; Wei, H.; Na, T.; Sun, H.; Zhang, H.; Yang, B. High-Efficiency Aqueous-Processed Hybrid Solar Cells with an Enormous Herschel Infrared Contribution. *ACS Appl. Mater. Interfaces* **2014**, *6*, 8606−8612.

DOI: 10.1021/acsami.5b07197
ACS Appl. Mater. Interfaces 2015, 7, 23223−23230